



This open access document is posted as a preprint in the Beilstein Archives at <https://doi.org/10.3762/bxiv.2021.90.v1> and is considered to be an early communication for feedback before peer review. Before citing this document, please check if a final, peer-reviewed version has been published.

This document is not formatted, has not undergone copyediting or typesetting, and may contain errors, unsubstantiated scientific claims or preliminary data.

Preprint Title Local strain and tunneling current modulated excitonic luminescence in MoS₂ monolayers

Authors Yalan Ma, Romana A. Kalt and Andreas Stemmer

Publication Date 22 Dez. 2021

Article Type Full Research Paper

Supporting Information File 1 SupportingInformation.docx; 1.4 MB

ORCID® iDs Yalan Ma - <https://orcid.org/0000-0002-4772-7042>

Local strain and tunneling current modulated excitonic luminescence in MoS₂ monolayers

Yalan Ma^{*1}, Romana Alice Kalt¹, and Andreas Stemmer^{*1}

Address: ¹Nanotechnology Group, ETH Zürich, Säumerstrasse 4, 8803, Rüslikon, Switzerland

Email: Yalan Ma^{*} - mayala@ethz.ch, Andreas Stemmer^{*} - astemmer@ethz.ch

^{*} Corresponding author

Abstract

The excitonic luminescence of monolayer molybdenum disulfide (MoS₂) on a gold substrate is studied by scanning tunneling microscopy (STM). STM-induced light emission (STM-LE) from MoS₂ is assigned to the radiative decay of *A* and *B* excitons. The intensity ratio of *A* and *B* exciton emission can be modulated by the tunneling current, since the *A* exciton emission intensity saturates at high tunneling currents. Moreover, the corrugated gold substrate introduces local strain to the monolayer MoS₂, resulting in significant changes of electronic bandgap and valence band splitting. The modulation rates of strain on *A* and *B* exciton energies are estimated as -72 meV/% and -57 meV/%, respectively. STM-LE provides a direct link between exciton energy and local strain in monolayer MoS₂ with a spatial resolution <10 nm.

Keywords

Transition metal dichalcogenides (TMDCs); scanning tunneling microscopy (STM); excitonic luminescence; local strain; exciton-exciton annihilation

Introduction

Two-dimensional (2D) monolayer transition metal dichalcogenides (TMDCs), such as molybdenum disulfide (MoS_2) or tungsten diselenide (WSe_2), show semiconducting properties with direct electronic band gaps in the near-infrared to visible spectral region [1-3]. Moreover, monolayer TMDCs possess > 0.5 eV exciton binding energies [4-6], high quantum efficiencies [7,8] and valley selective circular dichroism [9,10]. These unique optical properties of monolayer TMDCs are promising for applications in optoelectronic devices, such as light-emitting devices [11-13] and photon-detectors [7,14-16]. The electronic band structures of monolayer TMDCs can be tuned by applying mechanical strain [17,18]. Thus, strain engineering has been reported to modify the optoelectronic responses of TMDCs, not only by controlling the magnitude of the strain [19,20] but also by controlling the spatial distribution [21,22], as proven by photoluminescence and Raman spectroscopy. However, far-field optical excitation methods are limited in providing information on the nanometer scale due to the diffraction of light.

One promising technique to overcome limitations in spatial resolution is light emission induced by scanning tunneling microscopy (STM). The STM tip works as a low-energy electron source that excites the sample locally. Recently, STM-induced light emission (STM-LE) has been applied to detect excitonic luminescence in monolayer MoSe_2 [23,24], tunneling-current-controlled charged and neutral exciton emission in

monolayer WSe₂ [25], radiative plasmonic modes in free-standing monolayer MoS₂ [26], and photon emission from atomic defects in monolayer WS₂ [27].

In this work, we studied the excitonic luminescence of monolayer MoS₂ by STM-LE. The monolayer MoS₂ flakes synthesized by chemical vapor deposition (CVD) are transferred onto evaporated gold thin film substrates and excited locally by the STM tunneling electrons. The STM-LE spectra show typical characteristics of radiative decay of *A* and *B* excitons. An intensity saturation of *A* exciton emission is observed when increasing the tunneling current, which can be assigned to exciton-exciton annihilation [28-30]. Thus, by adjusting the tunneling current one can control the ratio of *B* exciton to *A* exciton emission.

Moreover, due to the strong van der Waals interactions, the monolayer MoS₂ conforms to the corrugated Au surface, resulting in locally varying strain in MoS₂. We observe significant peak (exciton energy) shifts in STM-LE spectra caused by these local strains in MoS₂. In addition, the valence band splitting is found to be modulated by the strain. We report the first observation of local strain-modulated excitonic luminescence in monolayer MoS₂ by STM-LE, with a spatial resolution < 10 nm. The STM-LE technique offers an efficient approach to studying the optical properties of 2D materials on the nanometer scale.

Results

Basic characterization

Figure 1a shows an optical image of triangular-shaped monolayer MoS₂ flakes transferred onto the evaporated Au substrate. The substrate provides enough visual contrast between Au and MoS₂ to unambiguously identify MoS₂ flakes. Figure 1b shows the surface topography of a monolayer MoS₂ flake acquired by atomic force

microscopy (AFM) in tapping mode. Figure 1c displays a constant-current STM image of the same MoS₂ flake at higher magnification. The monolayer MoS₂ is confirmed by the AFM profile, which shows a step height of ~ 1nm for a single layer. The surface corrugation of the underlying evaporated Au film translates into MoS₂, as evidenced by the STM topography and confirmed by AFM. As a result, local variations in deformation and strain are to be expected in the monolayer MoS₂.

We now turn to the characterization of electronic properties of monolayer MoS₂ by scanning tunneling spectroscopy (STS) (see Figure 1d). The reference dI/dV spectrum on bare Au surface shows the characteristic surface state at around 0.50 V tip bias. The dI/dV spectrum of MoS₂ displays clear band edges: conduction band minimum (CBM) and valence band maximum (VBM) at -0.80 V and 1.51 V, respectively, indicating the electronic band gap of the monolayer MoS₂ to be 2.31 eV. Figure 1e compares the STM-LE spectra of the monolayer MoS₂/Au and the bare Au surface. Since Pt and Ir of the STM tip are considered non-plasmonic materials due to their large imaginary part of the dielectric constants in visible/NIR regime [31], light emission from the Au surface is attributed to the surface plasmonic radiative mode. The STM-LE spectrum of monolayer MoS₂ shows a typical peak at 1.80 eV from radiative recombination of A exciton [2], indicating a 0.51 eV A exciton binding energy (i.e., energy difference between electronic band gap and optical gap).

In addition, the photon emission quantum efficiency of MoS₂ is obtained by simultaneously scanning the sample surface with STM tip and recording the photon number with the photon counter. With a tip bias of -3.25 V, the averaged photon count is 350 s⁻¹nA⁻¹ (Figure S1). Accounting for the geometric collection efficiency of the lens system and the photon counter's detection efficiency, the quantum efficiency (QE) of STM-LE of monolayer MoS₂ is estimated to be 3.7x10⁻⁶ photons per electron.

Tunneling current-induced exciton emission

Exciton emission of TMDCs has been reported to depend on current. Examples include multiple-exciton-exciton interactions in a MoS₂ diode [30] and neutral exciton and trion emission controlled by tunneling current [25]. Using STM-LE, we studied the influence of local tunneling current and tip bias on exciton emission from monolayer MoS₂. The STM-LE spectra acquired at a fixed sample location with a constant tip bias are shown in Figure 2a. The spectra indicate a systematic change of exciton emission with different current settings. When the tunneling current is around 20 nA, the spectrum only shows one emission peak, corresponding to the *A* exciton recombination. A secondary emission peak, blue-shifted by 0.20 eV from the *A* peak, appears for higher tunneling currents. This energy shift matches the valence band splitting energy induced by strong spin-orbit coupling in monolayer MoS₂ [32,33]. Hence, the secondary spectral peak is assigned to the radiative decay of *B* excitons. Tunneling current only influences the exciton emission intensity but not the exciton energy, as the spectral peaks do not shift with different current settings. Figure 2b further demonstrates that the tip bias does not affect the exciton energy.

Understanding the exciton dynamics of monolayer MoS₂ is essential for device development. The current-dependent emission intensities of *A* and *B* excitons are presented in Figure 2c,d. The STM-LE intensity is related to the exciton lifetime (τ_{ex}), which depends on the radiative and nonradiative exciton decay through [34]:

$$\frac{1}{\tau_{\text{ex}}} = \frac{1}{\tau_{\text{r}}} + \frac{1}{\tau_{\text{nr}}},$$

where τ_{r} and τ_{nr} are the radiative and non-radiative decay times, respectively. The STM-LE intensity is proportional to $\frac{\tau_{\text{ex}}}{\tau_{\text{r}}}$ [34]. Radiative recombination rate is an intrinsic property, which shows little change from sample to sample for the same material at a fixed temperature in similar environment [35]. The negligible changes of the peak

positions and full-width-half-maximums for both A and B exciton emissions indicate no heating effect on the sample through the measurements. Thus, the intensity difference among different sample locations for a given tunneling current (slopes in Figure 2d) is mainly caused by the non-radiative recombination associated with the local environment, for instance, local defect density [36] or substrate doping [37]. This is applicable for both A and B excitons.

In Figure 2, the B peak intensity shows a linear dependence on the tunneling current in the range of 20 nA ~ 60 nA. In contrast, A peak intensity saturates under high tunneling currents. This saturation of A peak intensity can be explained by the non-linear process of exciton-exciton annihilation (EEA), which has been widely observed in monolayer TMDCs in photoluminescence measurements [34,38]. For high exciton density, EEA opens an additional path for non-radiative exciton decay. In steady state, the rate of change in the population N of excitons excited by tunneling current injection can be described as [38]:

$$\frac{dN}{dt} = -\left(\frac{1}{\tau_{\text{ex}}}\right)N - \gamma_{\text{EEA}}N^2 + J,$$

where, γ_{EEA} is the EEA rate, and J is the injection-current-associated excitation. The STM-LE intensity is proportional to the exciton population N . When N is low, the exciton decay is determined by the linear radiative and non-radiative processes and the light intensity shows a linear dependence on the excitation current. When the exciton population is large ($N > \left(\frac{1}{\tau_{\text{ex}}}\right) / \gamma_{\text{EEA}}$), EEA becomes the major exciton decay process, causing the current-dependent STM-LE intensity to deviate from the linear trend.

In our measurements, the required injection current for A exciton to reach the EEA-dominated population regime is lower than that for B exciton. This difference can be explained by the different exciton lifetimes and EEA rates between A and B excitons. Particularly, the rapid relaxation (~ps) from B exciton to A exciton reduces the B exciton

population and simultaneously increases the A exciton population [39]. More quantitative analysis of exciton dynamics would require ultrafast time-resolved spectroscopy, which is beyond the scope of our setup. Knowing the EEA rate helps control the excitation injection to maintain an optimal light emission efficiency of TMDCs.

Strain-induced exciton emission

Monolayer MoS₂ exhibits high mechanical flexibility [40]. Placed on an evaporated Au substrate, van der Waals interactions make the monolayer MoS₂ conform to the local surface corrugation, which causes locally varying levels of strain. Strain tunes the electronic band gap but not the binding energy of excitons [17,18,41]. Thus, we observe significant peak shifts of exciton emission as shown in Figure 3, where STM-LE spectra are acquired at sample locations separated by 10 nm.

Low tunneling current

To identify the bandgap modulation by strain, we performed STM-LE on monolayer MoS₂ with low tunneling currents. Figure 4a shows an STM image of monolayer MoS₂ on Au substrate, acquired with constant tunneling current and tip bias. The AFM image of the same area, Figure 4b, shows identical surface structures. We conclude that the height information in STM image is determined by the surface topography of the monolayer MoS₂. The area marked by the white box in Figure 4a, which includes surfaces with different local curvatures, is evaluated by STM-LE. Figure 4c presents the STM-LE spectral map showing the peak wavelength of A excitons with pixel size of 10 x 10 nm². Figure 4d highlights four spectra acquired at positions with different local curvatures. The spectral shifts correlate with the local strain of the monolayer

MoS₂. A 44 nm red shift is observed between the locations with the highest and lowest strains.

To derive local strain from local surface topography, we estimate strain by comparing the surface area of MoS₂ and its projected area. To this end, a Gaussian filter is applied to the local surface topography to generate smooth surfaces. Then, the tensile strain is obtained by:

$$\text{strain} = \frac{\text{surface area} - \text{projected area}}{\text{projected area}} \times 100\%.$$

The relationship between the *A* exciton energy and the corresponding strain is shown in Figure 4e. The *A* exciton energy exhibits a linear dependence on the strain. The modulation rate of strain on *A* exciton energy shift is estimated to -70 ± 13 meV/% from linear fitting. This value is close to the results obtained by diffraction-limited photoluminescence of monolayer MoS₂ on patterned substrates [19,22]. Moreover, spectra acquired on other monolayer MoS₂ flakes transferred from the same CVD-synthesis have closely matching values for the strain modulation rates (Figure S4).

High tunneling current

We further investigated the influence of strain on the band structure of monolayer MoS₂ under high tunneling currents, where both *A* and *B* peaks are visible. In addition to modifying the bandgap, the strain could also affect band splitting. In Figure 5, STM-LE spectra are recorded on monolayer MoS₂ at locations with different surface curvatures (i.e., strain). The area for each location is 10 x10 nm². The local strain is calculated by the same method as described above. Both *A* and *B* exciton energies show linear dependences on strain, like the results obtained for low tunneling currents. The *B* exciton energy decreases with strain at a rate of -57 ± 11 meV/%, which is different from *A* exciton energy. This deviation between *A* and *B* exciton energy shifts provides

evidence that the valence band splitting changes with strain, which is consistent with theoretical calculations [41,42].

Discussion

Two possible excitation mechanisms can be involved in STM-LE: (i) diodelike excitation through electron and hole injections [25,43,44] and (ii) resonance energy transfer by virtual photon coupling [23]. The diodelike excitation mechanism generally requires a luminescent onset electron energy (i.e. tip bias) higher than the 'free particle' electronic bandgap energy of monolayer MoS₂. In the resonance energy transfer mechanism, the onset of luminescence occurs at an electron energy surpassing the optical gap energy. In our work, the onset of luminescence of MoS₂ occurs at a negative tip bias of -1.80 eV (Figure S2), close to the optical gap of monolayer MoS₂, indicating that the luminescence is excited by virtual photon coupling. Due to the limited sensitivity of our spectrometer, all STM-LE spectra were acquired with a tip bias higher than the electronic bandgap of monolayer MoS₂, where both excitation processes may be present.

In our measurements, STM-LE spectra show no systematic peak shifts at fixed locations for varying tip bias or tunneling current. Hence, the tunneling gap or the electrical field have little influence on the exciton energies of MoS₂. Furthermore, the plasmonic emission from the Au substrate shows a weak spectral signal, which is also different from the exciton emission in MoS₂ (see Figure 1 and Figure S3). The STM-LE intensity acquired on MoS₂ (Figure S2) displays an asymmetric dependence on the sign of the tip bias voltage, indicating that the plasmonic-exciton coupling between the Au substrate and monolayer MoS₂ is weak. Thus, the spectral shifts in excitonic luminescence in monolayer MoS₂ are directly related to alterations of the electronic

bandgap induced by strain. In strain engineered 2D materials, thermal scanning probe lithography has recently achieved a strain pattern with 20 nm resolution [22]. It is challenging to adequately resolve such a fine pattern by far-field optical excitation methods. Taking advantages of STM-LE, we demonstrate a spatial resolution of <10 nm in strain measurements on monolayer MoS₂, as evidenced in Figure 3.

Conclusion

STM-LE is a powerful technique to probe excitons in confined semiconductors with nanometer lateral resolution. In this work, we present a study of the excitonic luminescence of monolayer MoS₂ on an evaporated gold thin film substrate, locally excited by a non-plasmonic STM tip. The weak plasmonic coupling from the substrate allows one to investigate the native excitonic emission of monolayer MoS₂. The luminescent spectra from monolayer MoS₂ are attributed to the radiative recombination of *A* and *B* excitons. Both *A* and *B* excitonic peaks show energy shifts due to the local strain introduced by the corrugated substrate. Additionally, the emission intensities of *A* and *B* excitons depend on tunneling current. Thus, by tuning the tunneling current, the luminescence spectra can be adapted to different investigations. For instance, the local strain distribution of monolayer MoS₂ can be probed with a low tunneling current through analyzing the *A* exciton energy, which avoids long-term heating. Exciton energies and dynamics (in particular, exciton lifetimes) can be explored with high tunneling currents, where both *A* and *B* exciton emissions are detectable. In addition to investigating the optoelectronic properties of 2D materials, STM-LE also enables one to perform local analyses of strain or material deformation in piezoelectrical [45,46] and piezo-resistive devices [47].

Experimental

Materials

Sulfur (S) powder (99.98 %, Sigma-Aldrich, CAS: 7704-34-9) and sodium molybdate (Na_2MoO_4) powder (≥ 98 %, Sigma-Aldrich, CAS: 7631-95-0) were used as delivered and not purified further. The MoS_2 flakes were grown on a Si (100) n-type substrate, covered with a 300 nm thick SiO_2 layer, and synthesized in a 1-inch single heating zone tube furnace (Lindberg/Blue M). Quality and thickness of flakes were investigated by optical microscopy and atomic force microscopy.

Methods

CVD Synthesis

The Si/ SiO_2 substrate was cleaned in an ultrasonic bath with acetone, isopropanol (IPA), and de-ionized (DI) water for 15 to 20 minutes. Prior to placing the molybdenum source directly onto the cleaned substrate by spin-coating an aqueous Na_2MoO_4 solution, the substrate was treated with O_2 plasma to increase the hydrophilicity. The substrate was positioned at the center of the furnace, and 2 g of sulfur were placed in a crucible at the entrance of the furnace in the upstream heating zone. After the substrate and sulfur were loaded, the tube was flushed with 500 and 100 sccm N_2 before the start of the heating process and during the synthesis, respectively. The temperature was gradually increased to 750 °C within 20 minutes and held for 15 minutes before cooling down. To accelerate the cooling, the furnace was opened partly at 650 °C and completely at 570 °C.

Transfer

The flakes grown on Si/ SiO_2 were transferred onto an evaporated gold substrate (100 nm Au on SiO_2) with a modified polymethyl methacrylate (PMMA) mediated transfer

method [48]. To this end, the growth substrate was covered with PMMA (950k) by spin-coating. After curing overnight, the edges of the substrate were cut to increase the penetration of liquid and to cut off the flakes grown under the influence of the substrate edge. To peel off the PMMA layer, the substrate was floated on a 2 M KOH solution. Afterwards, the PMMA layer was washed three times with DI water before being transferred to a fresh gold substrate and dried overnight. To dissolve the PMMA layer, the gold substrate was immersed in acetone, IPA, and DI water for 1 minute per solvent for three cycles.

STM-LE Setup

STM-LE experiments were conducted at room temperature in high vacuum (10^{-7} mbar), using a custom-built STM instrument. An objective (Olympus LMPLFLN20x) inside the vacuum chamber plus a tube lens and camera mounted outside, serve to locate the samples from the top. An achromatic lens (Thorlabs A110-B, NA 0.4) mounted at an incident angle of 60° from the sample normal collects the emitted light. In the case of isotropic radiation, the hemisphere photon collection efficiency is about 8.3%. However, the light emission pattern is modified by the tip-sample junction and the orientations of the luminescent exciton/dipole [49,50]. Thus, the collection efficiency could be higher due to the angle-dependent emission pattern. In our experiments, we estimate the final detection efficiency of the optical system by only considering isotropic radiation. An optical fiber (Schaefer+Kirchhoff V-KF40-2x-MMC-VIS/NIR-105-NA022) guides the light out of the vacuum chamber to detectors. The STM-LE is either recorded by a photon counter (Hamamatsu C1300-1) or a spectrograph (Princeton Instrument SP2156i, with a 150 lines/mm grating) and a cooled CCD camera (PCO 2000). The differential conductance dI/dV is measured by STS with a lock-in amplifier (modulation voltage: 50 mV, and frequency: 470 Hz). All STM measurements are

acquired with platinum/iridium (90:10) tips prepared by electrochemical etching in CaCl_2 solution. Additionally, surface topography is acquired by an atomic force microscope (AFM) (Oxford Instruments, Cypher).

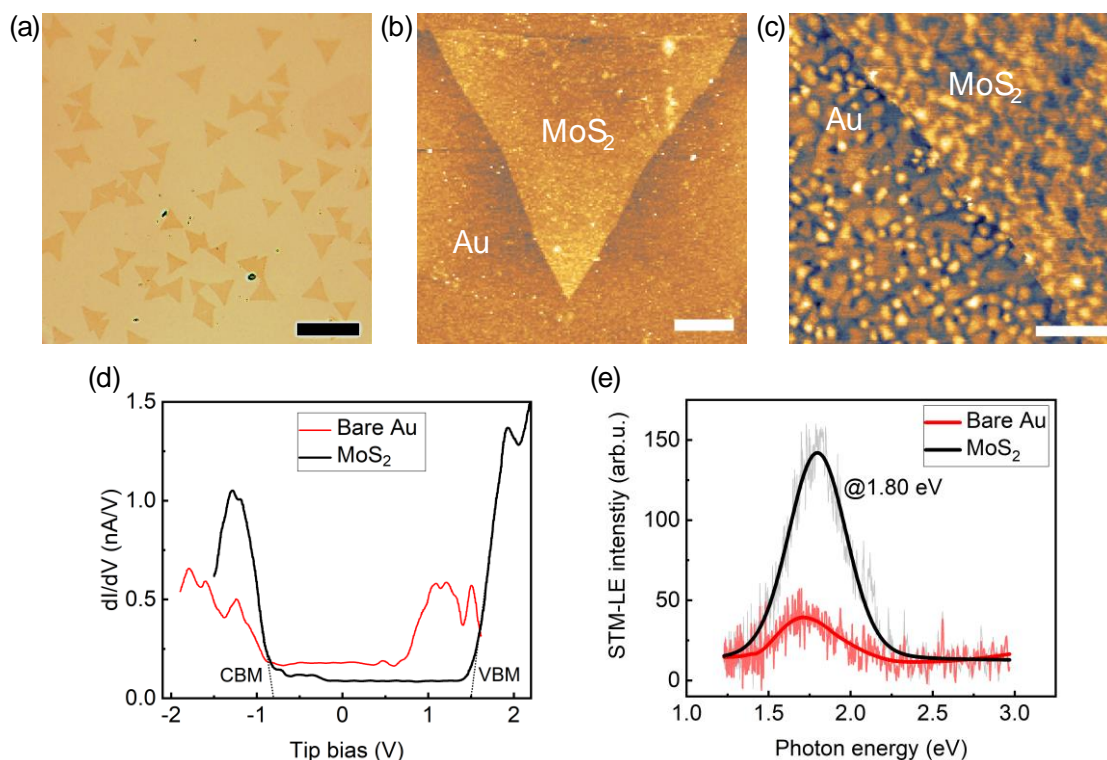


Figure 1: (a) Light microscopy image of typical CVD-synthesized monolayer MoS_2 flakes transferred onto the evaporated gold substrate. Scale bar: $20\ \mu\text{m}$. (b) AFM topography of a monolayer MoS_2 flake on the gold substrate. Scale bar: $2\ \mu\text{m}$. (c) STM topography obtained with a tip bias of $-3\ \text{V}$ and a tunneling current of $100\ \text{pA}$. Scale bar: $200\ \text{nm}$. (d) Differential conductance dI/dV spectra acquired on the bare gold surface and monolayer MoS_2 . The corresponding CBM and VBM, indicated by linear fits, are found at tip bias of $-0.80\ \text{eV}$ and $1.51\ \text{eV}$, respectively. (e) STM-LE spectra acquired on the bare gold substrate and MoS_2 at the same location as (d), with a tip bias of $-3\ \text{V}$ and a tunneling current of $30\ \text{nA}$. Integration time is $3\ \text{min}$.

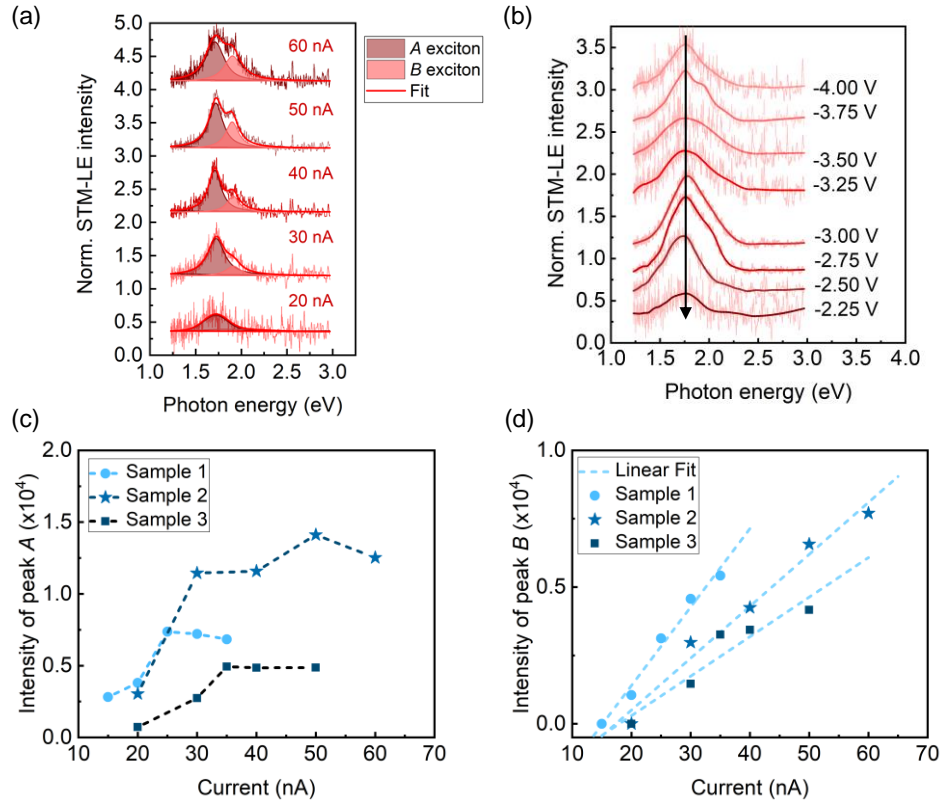


Figure 2: The influences of tunneling current and tip bias on STM-LE spectra of monolayer MoS₂. (a) Normalized STM-LE spectra acquired at a fixed sample location with different tunneling currents. Tip bias: -4 V. The spectra are well fitted with two Lorentzian peaks associated with A exciton (dark pink) and B exciton (light pink). (b) Normalized STM-LE spectra at a fixed sample location of MoS₂ with varying tip biases. Tunneling current: 30 nA. (c) and (d) show the current-dependent intensities for A and B excitons, respectively. The intensities are extracted from the fitted spectra obtained at different locations on the same MoS₂ flake. The data in (d) is fitted linearly.

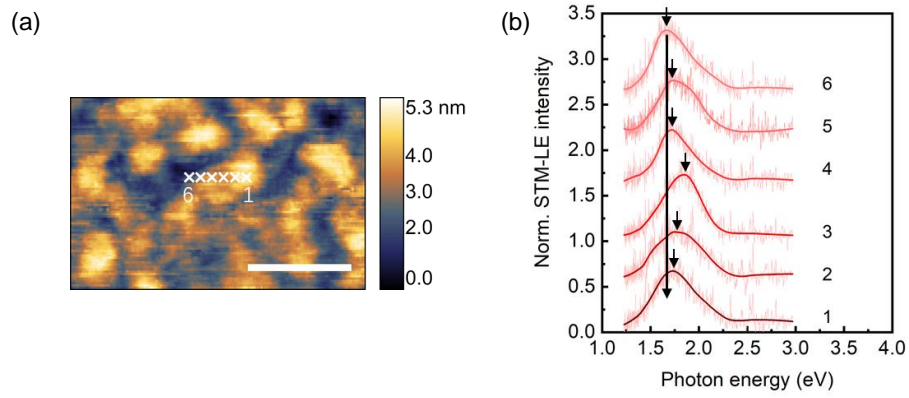


Figure 3: The influence of substrate topography on STM-LE spectra of monolayer MoS₂. (a) and (b) show STM topography and STM-LE spectra, respectively. The spectra are obtained at six sample locations separated by 10 nm as marked in (a). STM parameters: -3 V tip bias, and 100 pA tunneling current. Scale bar: 100 nm. STM-LE parameters: -4 V tip bias, 30 nA tunneling current, and 3 min integration time.

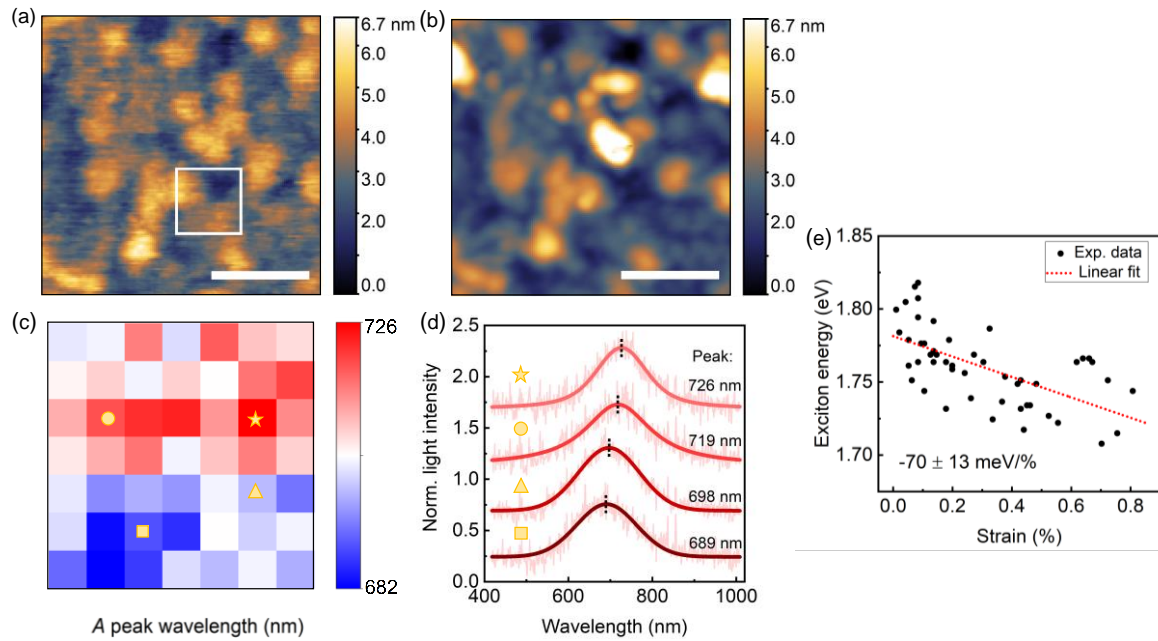


Figure 4: The influence of strain on STM-LE spectra of MoS₂. (a) STM image of monolayer MoS₂ acquired with a tip bias of -3 V and a tunneling current of 100 pA. Scale bar: 100 nm. (b) AFM image of MoS₂ at the same sample region as (a). Scale bar: 100 nm. (c) A peak wavelength map acquired at the region indicated in (a) by the white box. The pixel size is 10 x 10 nm². (d) STM-LE spectra obtained at locations marked in (c). STM-LE parameters: -4 V tip bias, 30 nA tunneling current, and 3 min integration time. (e) The distribution of A exciton energy as a function of strain. A linear fit is applied, resulting in a modulation rate of -70 ± 13 meV/%.

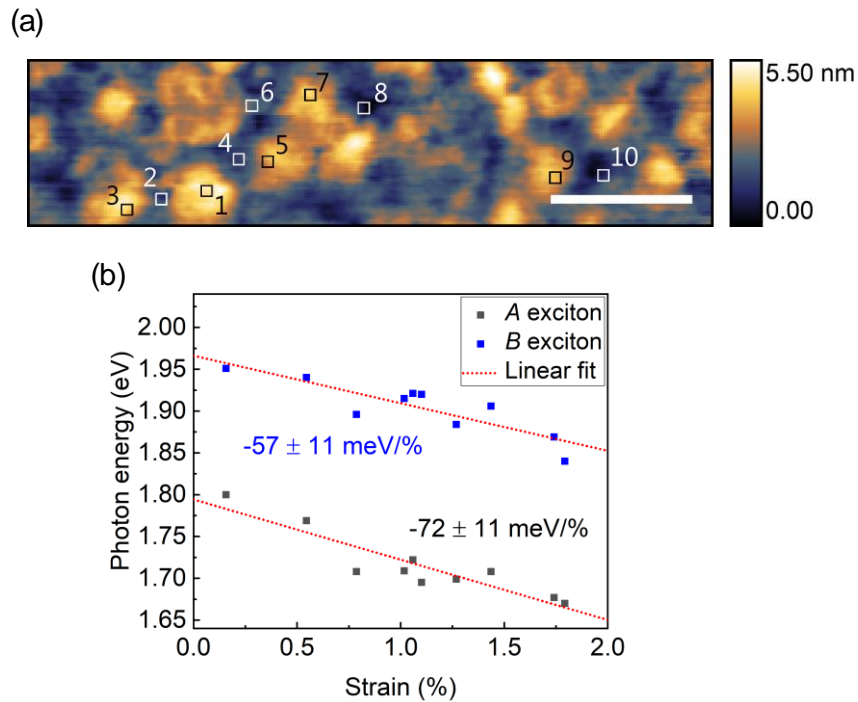


Figure 5: Strain-modulated *A* and *B* excitonic luminescence. (a) STM image of monolayer MoS₂ on Au surface. Tip bias: -3 V, tunneling current: 100 pA, scale bar: 100 nm. (b) *A* and *B* exciton energies as functions of strain, acquired at the locations indicated by the boxes in (a). Tip bias: -4 V, tunneling current: 50 nA, integration time: 3 min.

Supporting Information

Supporting information.pdf

Acknowledgement

The authors gratefully acknowledge the technical support of Blerim Veselaj (Nanotechnology Group, ETH Zurich), and the support of the BRNC cleanroom staff.

References

1. Splendiani, A.; Sun, L.; Zhang, Y.; Li, T.; Kim, J.; Chim, C. Y.; Galli, G.; Wang, F. *Nano Lett.* **2010**, *10*, 1271–1275.
2. Mak, K. F.; Lee, C.; Hone, J.; Shan, J.; Heinz, T. F. *Phys. Rev. Lett.* **2010**, *105*, 136805.
3. Zhao, W.; Ghorannevis, Z.; Chu, L.; Toh, M.; Kloc, C.; Tan, P. H.; Eda, G. *ACS Nano* **2013**, *7*, 791-797.
4. Cheiwchanchamnangij, T.; Lambrecht, W. R. L. *Phys. Rev. B* **2012**, *85*, 205302.
5. Chernikov, A.; Berkelbach, T. C.; Hill, H. M.; Rigosi, A.; Li, Y.; Aslan, O. B.; Reichman, D. R.; Hybertsen, M. S.; Heinz, T. F. *Phys. Rev. Lett.* **2014**, *113*, 076802.
6. He, K.; Kumar, N.; Zhao, L.; Wang, Z.; Mak, K. F.; Zhao, H.; Shan, J. *Phys. Rev. Lett.* **2014**, *113*, 026803.
7. Lopez-Sanchez, O.; Lembke, D.; Kayci, M.; Radenovic, A.; Kis, A. *Nature Nanotech.* **2013**, *8*, 497-501.
8. Amani, M.; Lien, D. H.; Kiriya, D.; Xiao, J.; Azcatl, A.; Noh, J.; Madhvapathy, S. R.; Addou, R.; KC, S.; Dubey, M.; Cho, K.; Wallace, R. M.; Lee, S. C.; He, J. H.; Ager, J. W.; Zhang, X.; Yablonovitch, E.; Javey, A. *Science* **2015**, *350*, 1065-1068.
9. Xiao, D.; Liu, G.-B.; Feng, W.; Xu, X.; Yao, W. *Phys. Rev. Lett.* **2012**, *108*, 196802.
10. Xu, X.; Yao, W.; Xiao, D.; Heinz, T. F. *Nature Physics* **2014**, *10*, 343-350.
11. Pospischil, A.; Furchi, M. M.; Mueller, T. *Nature Nanotech.* **2014**, *9*, 257-261.
12. Ross, J. S., Klement, P., Jones, A. M., Ghimire, N. J., Yan, J., Mandrus, D. G., Taniguchi, T.; Watanabe, K.; Kitamura, K.; Yao, W.; Cobden, D. H.; Xu, X. *Nature Nanotech.* **2014**, *9*, 268-272.
13. Zhang, Y. J.; Oka, T.; Suzuki, R.; Ye, J. T.; Iwasa, Y. *Science* **2014**, *344*, 725-728.

14. Yin, Z.; Li, H.; Li, H.; Jiang, L.; Shi, Y.; Sun, Y.; Lu, G.; Zhang, Q.; Chen, X.; Zhang, H. *ACS Nano* **2012**, *6*, 74-80.
15. Britnell, L.; Ribeiro, R. M.; Eckmann, A.; Jalil, R.; Belle, B. D.; Mishchenko, A.; Kim, Y. -J.; Gorbachev, R. V.; Georgiou, T.; Morozov, S. V.; Grigorenko, A. N.; Geim, A. K.; Casiraghi, C.; Castro Neto, A. H.; Novoselov, K. S. *Science* **2013**, *340*, 1311-1314.
16. Kufer, D.; Konstantatos, G. *Nano Lett.* **2015**, *15*, 7307-7313.
17. Scalise, E.; Houssa, M.; Pourtois, G.; Afanas'ev, V.; Stesmans, A. *Nano Research* **2012**, *5*, 43-48.
18. Castellanos-Gomez, A.; Roldán, R.; Cappelluti, E.; Buscema, M.; Guinea, F.; van der Zant, H. S. J.; Steele, G. A. *Nano Lett.* **2013**, *13*, 5361-5366.
19. He, K.; Poole, C.; Mak, K. F.; Shan, J. *Nano Lett.* **2013**, *13*, 2931-2936.
20. Conley, H. J.; Wang, B.; Ziegler, J. I.; Haglund Jr, R. F.; Pantelides, S. T.; Bolotin, K. I. *Nano Lett.* **2013**, *13*, 3626-3630.
21. Li, H.; Contryman, A. W.; Qian, X.; Ardakani, S. M.; Gong, Y.; Wang, X.; Weisse, J. M.; Lee, C. H.; Zhao, J.; Ajayan, P. M.; Li, J.; Manoharan, H. C.; Zheng, X. *Nature Communications* **2015**, *6*, 1-7.
22. Liu, X.; Sachan, A. K.; Howell, S. T.; Conde-Rubio, A.; Knoll, A. W.; Boero, G.; Zenobi, R.; Brugger, J. *Nano Lett.* **2020**, *20*, 8250-8257.
23. Pommier, D.; Bretel, R.; López, L. E. P.; Fabre, F.; Mayne, A.; Boer-Duchemin, E.; Dujardin, G.; Schull, G.; Berciaud, S.; Le Moal, E. *Phys. Rev. Lett.* **2019**, *123*, 027402.
24. Péchou, R.; Jia, S.; Rigor, J.; Guillermet, O.; Seine, G.; Lou, J.; Large, N.; Mlayah, A.; Coratger, R. *ACS Photonics* **2020**, *7*, 3061-3070.
25. Román, R. J. P.; Auad, Y.; Grasso, L.; Alvarez, F.; Barcelos, I. D.; Zagonel, L. F. *Nanoscale* **2020**, *12*, 13460-13470.
26. Krane, N.; Lotze, C.; Läger, J. M.; Reecht, G.; Franke, K. J. *Nano Lett.* **2016**, *16*, 5163-5168.

27. Schuler, B.; Cochrane, K. A.; Kastl, C.; Barnard, E. S.; Wong, E.; Borys, N. J.; Schwartzberg, A. M.; Ogletree, D. F.; de Abajo, F. J. G.; Weber-Bargioni, A. *Science Advances* **2020**, *6*, eabb5988.
28. Ma, Y. Z.; Valkunas, L.; Dexheimer, S. L.; Bachilo, S. M.; Fleming, G. R. *Phys. Rev. Lett.* **2005**, *94*, 157402.
29. Wang, F.; Wu, Y.; Hybertsen, M. S.; Heinz, T. F. *Phys. Rev. B*, **2006**, *73*, 245424.
30. Ye, Y.; Ye, Z.; Gharghi, M.; Zhu, H.; Zhao, M.; Wang, Y.; Yin, X.; Zhang, X. *Appl. Phys. Lett.* **2014**, *104*, 193508.
31. Fojtik, P.; Perronet, K.; Pelant, I.; Chval, J.; Charra, F. *Surface science* **2003**, *531*, 113-122.
32. Coehoorn, R.; Haas, C.; de Groot, R. A. *Phys. Rev. B* **1987**, *35*, 6203.
33. Zhao, W.; Ribeiro, R. M.; Toh, M.; Carvalho, A.; Kloc, C.; Castro Neto, A. H.; Eda, G. *Nano Lett.* **2013**, *13*, 5627-5634.
34. Yuan, L.; Huang, L. *Nanoscale* **2015**, *7*, 7402-7408.
35. Palumbo, M.; Bernardi, M.; Grossman, J. C. *Nano Lett.* **2015**, *15*, 2794-2800.
36. Wang, H.; Zhang, C.; Rana, F. *Nano Lett.* **2015**, *15*, 339-345.
37. Yu, Y.; Yu, Y.; Xu, C.; Cai, Y. Q.; Su, L.; Zhang, Y.; Zhang, Y. W.; Gundogdu, K.; Cao, L. *Adv. Funct. Mater.* **2016**, *26*, 4733-4739.
38. Yu, Y.; Yu, Y.; Xu, C.; Barrette, A.; Gundogdu, K.; Cao, L. *Phys. Rev. B* **2016**, *93*, 201111.
39. McCreary, K. M.; Hanbicki, A. T.; Sivaram, S. V.; Jonker, B. T. *APL Materials* **2018**, *6*, 111106.
40. Pu, J.; Yomogida, Y.; Liu, K. K.; Li, L. J.; Iwasa, Y.; Takenobu, T. *Nano Lett.* **2012**, *12*, 4013-4017.
41. Cheiwchanchamnangij, T.; Lambrecht, W. R. L.; Song, Y.; Dery, H. *Phys. Rev. B* **2013**, *88*, 155404.

42. Guo, S. D. *Computational Materials Science* **2016**, *123*, 8-13.
43. Qiu, X. H.; Nazin, G. V.; Ho, W. *Science* **2003**, *299*, 542-546.
44. Cheng, R.; Li, D.; Zhou, H.; Wang, C.; Yin, A.; Jiang, S.; Liu, Y.; Chen, Y.; Huang, Y.; Duan, X. *Nano Lett.* **2014**, *14*, 5590-5597.
45. Zhu, H.; Wang, Y.; Xiao, J.; Liu, M.; Xiong, S.; Wong, Z. J.; Ye, Z.; Ye, Y.; Yin, X.; Zhang, X. *Nature Nanotech.* **2015**, *10*, 151-155.
46. Wang, X.; He, X.; Zhu, H.; Sun, L.; Fu, W.; Wang, X.; Hoong, L. C.; Wang, H.; Zeng, Q.; Zhao, W.; Wei, J.; Jin, Z.; Shen, Z.; Liu, J.; Zhang, T.; Liu, Z. *Science Advances* **2016**, *2*, e1600209.
47. Li, W.; Dai, M.; Hu, Y.; Chen, H.; Zhu, X.; Yang, Q.; Hu, P. *ACS Appl. Mater. Interfaces* **2019**, *11*, 47098-47105.
48. Jiao, L.; Fan, B.; Xian, X.; Wu, Z.; Zhang, J.; Liu, Z. *J. Am. Chem. Soc.* **2008**, *130*, 12612-12613.
49. Schuller, J. A.; Karaveli, S.; Schiros, T.; He, K.; Yang, S.; Kymissis, I.; Shan, J.; Zia, R. *Nature Nanotech.* **2013**, *8*, 271-276.
50. Martin, O. J.; Girard, C. *Appl. Phys. Lett.* **1997**, *70*, 705-707.